FLUTTER BOUNDARY PREDICTION FOR A TWIN-ENGINE TRANSPORT FLUTTER MODEL USING A LINEARIZED UNSTEADY SOLVER

Shuchi Yang[1], Zhicun Wang[1], Zhichao Zhang[1], and P.C. Chen[1]

[1] ZONA Technology, Inc.
Scottsdale, Arizona
info@zonatech.com

2

Keywords: Aeroelasticity, Linearized Unsteady Solver, Transpiration Boundary Condition, Generalized Aerodynamic Forces.

Abstract: A linearized unsteady solver, referred to as ZONA Unstructured Linearized Unsteady Solver (ZULUS), is developed to solve the linearized frequency-domain unsteady equation on an unstructured mesh using the steady background flow solution generated by the Navier-Stokes (N-S) solver. ZULUS can generate an accurate frequency-domain Generalized Aerodynamic Forces (GAF) in the small perturbation sense about a nonlinear steady flow condition with a transpiration boundary condition that is applied to the stationary surface mesh. The GAF can be directly plugged into the frequency-domain flutter solution techniques to generate flutter solutions rapidly. A linearized static aeroelastic analysis capability is also developed in ZULUS to include the static aeroelastic effects in the GAF. The measured flutter boundary of a twin-engine transport flutter model in the Transonic Dynamic Tunnel (TDT) of NASA Langley is used to validate ZULUS. It is found that the static aeroelastic effects have a major impact on the flutter boundary. With the static aeroelastic effects, the ZULUS' predicted flutter boundary correlates much better with the TDT measured data than that without the static aeroelastic effects.

1 INTRODUCTION

During the past several decades, many researchers have applied the Computational Fluid Dynamics (CFD) methods to solve the Navier-Stokes (N-S) equations coupled with structural equations for the prediction of aeroelastic response using time-accurate schemes. For instance, Bartels et al. [1] applied the FUN3D [2] N-S solver to compute the flutter boundary of a truss-braced wing and correlated the predicted results with the TDT data. However, these time-accurate schemes usually have the following technical issues:

(1) The computational time for the unsteady aerodynamic cases is at least 2~3 orders higher than that of the steady aerodynamics cases. For complex configurations, this long computational time is not acceptable for routine industrial aeroelastic analysis.

(2) The computational mesh must be deformed according to the structural deformation using a moving mesh algorithm. This moving mesh algorithm requires additional computational resources, and becomes very complex in dealing with the discontinuous displacement in mode shapes such as the control surface modes for which generating a computational mesh could be a very tedious effort.

(3) Only the flutter mode with the lowest flutter speed can be captured by the time-accurate schemes. This is because when this flutter speed is encountered, the time-domain response is a divergent motion and the computation cannot proceed to obtain all flutter modes with higher flutter speeds.

Therefore, the frequency-domain unsteady aerodynamic methods still are the preferred approach used by the aerospace industry. This is because these methods can generate the frequency-domain GAF that can directly lead to the frequency-domain equation of motion of the aeroelastic system that reads:

$$\left[-\omega^2\left[M_{hh}\right]+i\omega\left[C_{hh}\right]+\left[K_{hh}\right]-q_\infty\left[Q_{hh}(i\omega)\right]\right]\{\xi\}=q_\infty\left[\left[Q_{hc}(i\omega)\right]\{\delta\}+\left\{Q_{hg}(i\omega)\right\}w_g\right] \tag{1}$$

Where $[M_{hh}]$, $[C_{hh}]$, and $[K_{hh}]$ are the structural generalized mass, damping and stiffness matrices; respectively. $[Q_{hh}(i\omega)]$, $[Q_{hc}(i\omega)]$, and $\{Q_{hg}(i\omega)\}$ are the GAFs due to structural modes, control surface kinematic modes and sinusoidal gust, respectively, generated by the frequency-domain unsteady aerodynamic methods. $\{\xi\}$is the generalized modal coordinate vector, $\{\delta\}$is control surface deflection vector, w_g is the gust profile, and q_∞ is the dynamic pressure.

The left-hand side of equation (1), in fact, represents the flutter equation that can be solved by the p-k method [3] or the g-method [4] to calculate the flutter solution of all flutter modes. Equation (1) can be solved directly in the frequency domain to generate the time-domain aeroelastic responses due to pilot and control system input commands and gust excitation using the inverse Fourier transform. Equation (1) also can be first recast in the state space equation by applying the Rational Function Approximation (RFA) to the GAF then used for flutter suppression or gust loads alleviation control law designs.

However, the frequency-domain unsteady aerodynamic methods used by the aerospace industry such as Doublet Lattice Method [5] and ZAERO [6] solve the linear potential equation that is not valid for nonlinear flows. In recent years, many researchers ([7], [8], [9], and [10]) have developed linearized Euler or N-S solvers to generate the GAF. These GAF also can be directly plugged into equation (1) to compute the aeroelastic responses that are valid in the entire Mach number range except in the small disturbance sense.

In this paper, we present a linearized unsteady solver, referred to as ZONA Unstructured Linearized Unsteady Solver (ZULUS), that solves the linearized frequency-domain unsteady equation on an unstructured mesh using the steady background flow solution generated by the N-S solver. To avoid the moving mesh issues, ZULUS employs the transpiration boundary condition that is applied to the stationary surface mesh. ZULUS has been validated with the wind tunnel data of various configurations ranging from simple wings like the Benchmark Active Controls Technology (BACT) wing [11,12] to complex configurations like the twin-engine transport flutter model [13].

2 FORMULATION OF THE LINEARIZED UNSTEADY SOLVER IN ZULUS

By applying the finite-volume method, the full Navier-Stokes equation can be represented by the following equation:

$$\partial Q/\partial t+\sum H_i S_i=\sum H_{vi} S_i \tag{2}$$

where the right-hand terms represent the viscous terms and the left-hand terms represent the unsteady variation and convection. The term S_i represents the surface vector from the cell.

Assuming that the structural oscillation amplitude to be small, then, the total unsteady terms can be split into to a steady part and an unsteady small perturbation part

$$Q = \bar{Q} + \tilde{Q}(t),\ H_i = \bar{H}_i + \tilde{H}_i(t),\ H_{v_i} = \bar{H}_{v_i} + \tilde{H}_{v_i}(t), \quad i = 1,2,3 \tag{3}$$

Substituting the above equations into the Equation (2) and assuming $\bar{Q} >> \tilde{Q}(t)$, $\bar{H}_i >> \tilde{H}_i(t)$ and $\bar{H}_{v_i} >> \tilde{H}_{v_i}(t)$ yield two sets of equations. The first is the steady part shown as follows:

$$\sum \bar{H}_i S_i = \sum \bar{H}_{vi} S_i \tag{4}$$

Equation (4) has the same form as Equation (2) except that the time derivative term is absent. Therefore, Equation (4) can be solved efficiently using the pseudo-time marching scheme.

The second set of equations is the linearized Navier-Stokes equation which reads

$$\partial \tilde{Q} / \partial t + \sum \left(\frac{\partial \bar{H}_i}{\partial Q} \tilde{Q} * S_i \right) = \sum \left(\frac{\partial \bar{H}_{vi}}{\partial Q} \tilde{Q} * S_i \right) \tag{5}$$

where $\frac{\partial \bar{H}_i}{\partial Q}$ is the mean flow convective flux Jacobians and $\frac{\partial \bar{H}_{vi}}{\partial Q}$ are the mean viscous flux Jacobians, referred to herein as the steady background flow. These Jacobians only includes the steady variables and are provided by equation (4). Applying Fourier transform, the frequency-domain counterpart of equation (5) reads:

$$i\omega \tilde{Q}(i\omega) + \sum \left(\frac{\partial \bar{H}_i}{\partial Q} \tilde{Q}(i\omega) * S_i \right) = \sum \left(\frac{\partial \bar{H}_{vi}}{\partial Q} \tilde{Q}(i\omega) * S_i \right) \tag{6}$$

Equation (6) is the linearized frequency-domain N-S equation that can generate the frequency-domain unsteady aerodynamic forces. However, directly solving equation (6) may have the following technical issues: (1) Solving Equation (6) requires the viscous mesh which needs to be much more refined than the inviscid mesh; leading to a much longer computational time than the linearized Euler solver, and (2) Since deriving the transpiration boundary condition for the N-S equation is very difficult and is currently not available, to solve Equation (6) requires the moving mesh algorithm. Thus, the technical issues associated with the moving mesh algorithm for solving the linearized N-S equation are the same as for solving the full unsteady N-S equation. To circumvent the above technical issues, we developed a hybrid approach by ignoring the viscous terms in the right-hand side of equation (6) which leads the linearized unsteady equation that reads:

$$i\omega \tilde{Q}(i\omega) + \sum \left(\frac{\partial \bar{H}_i}{\partial Q} \tilde{Q}(i\omega) * S_i \right) = 0 \tag{7}$$

Equation (7) is the frequency-domain linearized unsteady equation except that the steady background flow in terms of $\frac{\partial \bar{H}_i}{\partial Q}$ is externally provided by a steady N-S solver. Because of

the lack of the viscous terms like those on the Right-Hand Side (RHS) of Equation (5), Equation (7) can be solved using an inviscid mesh so that the long computational time required to solve the N-S equation can be avoided.

The unsteady flow structure is dominated by the steady flow structure in the small perturbation sense. Thus, if the steady flow solution is provided by a high fidelity flow solver such as the Reynolds-Averaged Navier-Stores (RANS) solver, the accurate unsteady flow solution is assured even using a lower fidelity linearized flow solver such as the linearized unsteady solver in ZULUS.

3 TRANSPIRATION BOUNDARY CONDITION

To solve the linearized unsteady equation, ZULUS employs the transpiration boundary condition that can avoid the issues associated with the moving mesh algorithm altogether. The transpiration boundary condition is a first order Taylor's expansion of the exact Euler boundary condition on the instantaneous moving surface $S(x,y,z,t)=0$ about the non-moving stationary position of the surface $S_0(x, y, z) = 0$. The transpiration boundary condition of the linearized Euler equation reads:

$$\begin{aligned}\tilde{w}_n(x,y,z,t)\big|_{s_0} &= \tilde{u}(x,y,z,t)\big|_{s_0}\,\partial S_o/\partial x + \tilde{v}(x,y,z,t)\big|_{s_0}\,\partial S_o/\partial y \\ &+ \bar{u}(x,y,z)\tilde{\phi}_x(x,y,z,t) + \bar{v}(x,y,z)\tilde{\phi}_y(x,y,z,t) + \dot{\tilde{\phi}}(x,y,z,t)/V\end{aligned} \tag{8}$$

where $\tilde{w}_n(x,y,z,t)$, $\tilde{u}(x,y,z,t,)$ and $\tilde{v}(x,y,z,t)$ are the unsteady perturbation velocity along the normal and tangential directions on the stationary surface mesh, $\bar{u}(x,y,z)$ and $\bar{v}(x,y,z)$ are the steady flow velocities along the tangential direction that are provided by the steady N-S solver and $\tilde{\phi}(x,y,z,t)$ is the structural mode shape or the control surface kinematic mode whose amplitude is assumed to be small and is used as the small parameter involved in the Taylor's expansion to derive the transpiration boundary condition.

Assuming the response to be a simple harmonic motion; i.e. $\tilde{w}_n(x,y,z,t) = w_n(x,y,z,i\omega)e^{i\omega t}$, $\tilde{u}(x,y,z,t) = u(x,y,z,i\omega)e^{i\omega t}$, $\tilde{v}(x,y,z,t) = v(x,y,z,i\omega)e^{i\omega t}$, and $\tilde{\phi}(x,y,z,t) = \phi(x,y,z,i\omega)e^{i\omega t}$, Equation (8) can be transformed into the frequency domain:

$$\begin{aligned}w_n(x,y,z,i\omega)\big|_{s_0} &= u(x,y,z,i\omega)\big|_{s_0}\,\partial S_o/\partial x + v(x,y,z,i\omega)\big|_{s_0}\,\partial S_o/\partial y \\ &+ \bar{u}(x,y,z)\phi_x(x,y,z,i\omega) + \bar{v}(x,y,z)\phi_y(x,y,z,i\omega) + i\omega\phi(x,y,z,i\omega)/V\end{aligned} \tag{9}$$

Because all terms involved in Equation (9) are evaluated on the stationary surface mesh, $S_0(x,y,z)=0$, no moving mesh is required for the transpiration boundary condition. Applying Equation (9) to the linearized unsteady equation yields the frequency-domain unsteady pressures and GAF due to structural mode shapes and control surface kinematic modes.

Incorporating the gust excitation into the transpiration boundary condition is very straightforward. The time-domain gust excitation for generating the elementary gust solution is a traveling Dirac delta function, $\delta(t-(x-x_0)/V)$, where x_0 is the reference point of the gust, V the free stream velocity and x is a point on the surface mesh like the one shown in Figure 1.

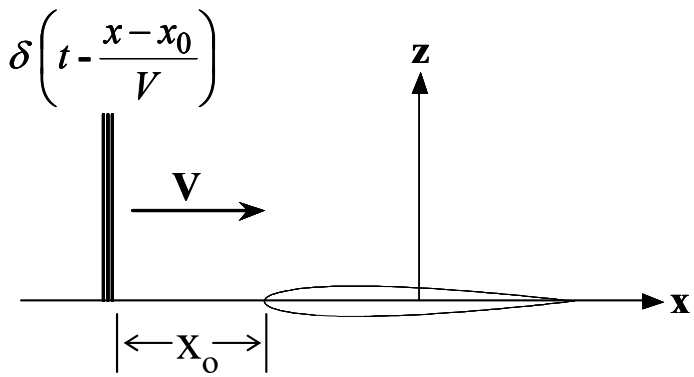

Figure 1: Traveling Dirac Delta Function for Elementry Gust Solution

The frequency-domain counterpart of the traveling Dirac function, which is usually called the sinusoidal gust, can be immediately obtained by Fourier transform:

$$\bar{\delta}(i\omega) = \int_{-\infty}^{\infty} \delta(t-(x-x_0)/V)e^{-i\omega t}dt = e^{-i\omega(x-x_0)/V} \tag{10}$$

The induced angle of attack due to the frequency-domain traveling Dirac delta function can be directly plugged into the transpiration boundary condition to yield the gust solution such as:

$$w_n(x,y,z,i\omega)\big|_{s_0} = u(x,y,z,i\omega)\big|_{s_0}\,\partial S_o/\partial x + v(x,y,z,i\omega)\big|_{s_0}\,\partial S_o/\partial y - \bar{u}(x,y,z)e^{-i\omega(x-x_0)/V} \tag{11}$$

Using equations (9) and (11), ZULUS can generate the GAF due to structural modes, $Q_{hh}(iw)$, and control surface kinematic modes, $Q_{hc}(iw)$, as well as due to sinusoidal gust, $Q_{hg}(iw)$, and consequently construct equation (1) to generate aeroelastic responses due to pilot and control system input commands and gust excitation.

4 THE LINEARIZED STATIC AEROELASTIC ANALYSIS CAPABILITY IN ZULUS

It is well known that the static aeroelastic effects may have a large impact on the flutter boundary, especially in the transonic flow regions. Ideally, a static aeroelastic analysis should be performed first by coupling the N-S solver with a structural solver to obtain a steady flow solution on an aeroelastically deformed shape. Then, providing this steady flow solution to ZULUS as the steady background flow leads to the GAF for flutter analysis with static aeroelastic effects. However, such a static aeroelastic analysis by coupling N-S solver with a structural solver may require a significant computational effort.

Using the GAF generated by ZULUS at zero reduced frequency (k), a linearized static aeroelastic analysis can be formulated to efficiently solve the static aeroelastic equation in the small perturbation sense. First, let the total aerodynamic forces be split into the aerodynamic forces on the rigid aircraft and aeroelastic incremental forces, then a linearized static aeroelastic equation can be constructed that reads:

$$[K]\{x\} = q_\infty\{F_0\} + q_\infty\{F_e(x)\} \tag{12}$$

where $[K]$ is the structural stiffness matrix, $q_\infty\{F_0\}$ is the aerodynamic forces on the rigid aircraft and $q_\infty\{F_e(x)\}$ is the incremental aerodynamic feedback forces due to the structural deformation $\{x\}$.

Assuming that the structural deformation can be super-imposed by the structural elastic mode shapes $[\phi_e]$, and the generalized modal coordinates $\{\xi\}$ of the elastic modes as follows:

$$\{x\} = [\phi_e]\{\xi\} \tag{13}$$

and pre-multiplying equation (12) by $[\phi_e]^T$ yields:

$$[K_{ee}]\{\xi\} = q[\phi_e]^T\{F_0\} + q[\phi_e]^T\{F_e(x)\} \tag{14}$$

where $[K_{ee}]$ is the generalized stiffness matrix of the elastic modes
Next, $\{F_e(x)\}$ can be super-imposed by the incremental aerodynamic feedback forces due to each structural mode, where $[f_i] = [f_1, f_2, \ldots, f_h]$ and the subscript h is the number of modes, shown as follows:

$$\{F_e(x)\} = [f_i]\{\xi\} \tag{15}$$

$[f_i]$ can be obtained by substituting each mode shape into the transpiration boundary condition of ZULUS at k=0. In fact, $[\phi_e]^T [f_i] = \mathrm{Re}[Q_{ee}(k = 0)]$ is the real part of Q_{ee} at k=0. Finally, a linearized static aeroelastic equation can be derived:

$$[[K_{ee}] - q_\infty \mathrm{Re}[Q_{ee}(k=0)]]\{\xi\} = q_\infty [\phi_e]^T\{F_0\} \tag{16}$$

In equation (16), $\{F_0\}$ can be obtained either by the N-S solver on the unformed mesh and $[Q_{ee}(k = 0)]$ is provided by ZULUS' linearized unsteady solver. Inverting the Left-Hand Side (LHS) matrix of Equation (16) yields $\{\xi\}$ that leads to the structural deformation $\{x\}$. It should be noticed that this matrix is singular when the dynamic pressure is one of the eigenvalues of the LHS matrix. This dynamic pressure is called the static divergence dynamic pressure. Thus, a static divergence analysis can be performed by computing the eigenvalues of this LHS matrix among which the smallest real positive eigenvalue is the lowest divergence dynamic pressure of the structure. Thus, if the input dynamic pressure for the static aeroelastic analysis is higher than the divergence dynamic pressure, the structure is aeroelastically unstable, and the result of the static aeroelastic analysis is physically meaningless.

After $\{\xi\}$ is obtained, the total perturbed conservative flow variables can be obtained by superimposing the perturbed conservative flow variables of each mode with $\{\xi\}$. Adding the superimposed perturbed conservative flow variables to those computed by the N-S solver yields the updated steady background flow solution with static aeroelastic effects that are provided to ZULUS linearized unsteady solver for computing the GAF.

The linearized static aeroelastic analysis is very computational efficient since $[Q_{ee}(k = 0)]$ can be provided by ZULUS with parallelized computation using Message Passing Interface (MPI) and solving equation (16) only involves the decomposition of the LHS matrix of equation (16) whose size is only the number of modes. Therefore, the linearized static aeroelastic analysis should always be performed first. Then, the updated steady background flow solution can be

rapidly generated to account for the static aeroelastic effects in the ZULUS to generate GAFs for flutter analysis.

5 VALIDATION OF THE ZULUS GUST SOLUTION WITH ZONA6

All Generation of the generalized aerodynamic forces due to gust (Q_{hg}) by ZULUS is very straightforward; simply adding the $e^{-i\omega(x-x_0)/V}$ term in the frequency-domain transpiration boundary condition. Using the rational function approximation, the Q_{hg}, Q_{hc}, and Q_{hh} matrices along with the structural generalized mass, stiffness and damping matrices can lead to the state-space equation that is the frequency-domain counterpart expressed in Equation (1) for performing the gust and ASE analysis. To form this state-space equation, we have integrated the gust module and the ASE module of ZAERO [14] into ZULUS. The integrated gust module and ASE module in ZULUS replace the Q_{hg} ,Q_{hc} and Q_{hh} matrices computed by the linear unsteady aerodynamic method such as ZONA6 [15] in ZAERO by those generated by ZULUS so that the difference in the gust and ASE solutions between ZAERO and ZULUS is purely due to the different unsteady aerodynamic matrices..

The test case selected for the gust analysis is the BACT wing at M=0.45 except that its *t/c* is reduced to 3%. Because of the thin airfoil section and the low Mach number, the ZAERO gust solution based on the linear unsteady aerodynamic method (ZONA6) is valid and can be used to validate the ZULUS gust solution.

5.1 Validation of ZULUS Discrete Gust Result

The discrete gust profile is a 1-cosine gust at V=508 fps and dynamic pressure (q)=129 psf with a gust velocity=25 fps and gust length=2.66 ft. The acceleration at the accelerometer located at the inboard of the wing trailing edge, wing root bending moment and wing root torsion are computed by ZULUS and ZAERO and are presented in Figure 2. This 1-cosine gust hits the leading edge of the BACT wing at time (t)=0, therefore, prior to t=0, no responses of the wing are observed. Excellent agreement between the ZAERO and ZULUS solutions is obtained which validates the discrete gust analysis capability of ZULUS.

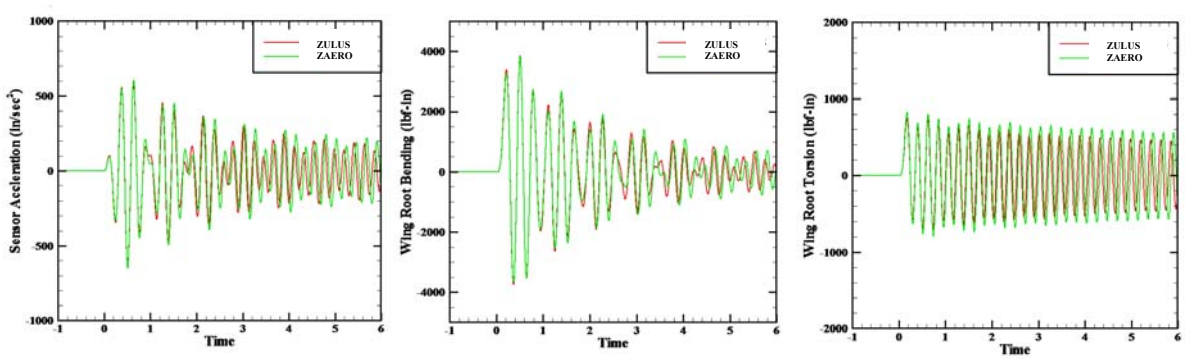

(a) Sensor Acceleration **(b) Wing Root Bending** **(c) Wing Root Torsion**

Figure 2: Discrete Gust Responses of BACT Wing due to 1-Cosine Gust Excitation at M=0.45 and q=129 psf.

5.2 Validation of ZULUS Continuous Gust Result

The Dryden's gust spectrum with Root-Mean-Square (RMS) gust velocity=25 fps is used for the continuous gust analysis. Figure 3 depicts the auto-Power Spectrum Density (PSD) of acceleration at the accelerometer, the wing root bending moment, and the wing root

torsion; and cross-PSD of the wing root bending moment and torsion computed by ZULUS and ZAERO in which excellent agreement between these two codes can be observed. It should be noted that the current FAA airworthiness requirement specifies the use of both discrete and continuous gust analyses. The continuous gust analysis using the linear unsteady aerodynamic methods is a routine practice in the aerospace industry. But such an analysis capability is currently not available in any CFD code; making ZULUS a unique tool for continuous gust analysis.

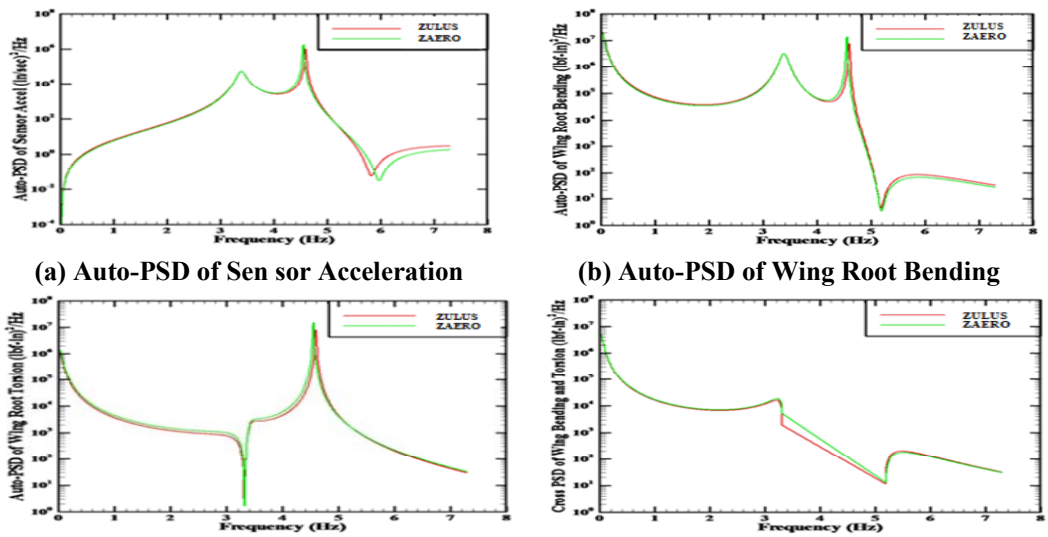

(a) Auto-PSD of Sen sor Acceleration **(b) Auto-PSD of Wing Root Bending**

(c) Auto-PSD of Wing Root Torsion **(d) Cross-PSD of Wing Bending and Torsion**

Figure 3: Continuous Gust Responses of BACT Wing due to Dryden's Gust Spectrum at M=0.45 and q=129 psf.

6 VALIDATION OF ZULUS PLANT MODEL GENERATION CAPABILITY WITH TRANSONIC DYNAMIC TUNNEL (TDT) DATA

To design an effective control system for flutter suppression and gust load alleviation, it requires an accurate plant model that relates the sensor output to the control input. The accuracy of the plant model can be characterized by comparing its frequency response to the test data in a wide range of frequencies. In order to validate the ZULUS plant model generation capability using the integrated ZAERO ASE module, the BACT wing on the Pitch and Plunge Apparatus (PAPA) flexible mount system is selected. Two sets of frequency responses at the accelerometer located at the inboard trailing edge of the wing were measured by the TDT testing; one due to the tailing edge flap input and the other due to the upper spoiler input. Waszak [16] also computed these two frequency responses using the wind tunnel measured aerodynamic force and moment stability derivatives due to the pitch and plunge modes as well as due to the trailing edge flap and upper spoiler inputs. The ZULUS results are obtained by the integrated ZAERO frequency-domain ASE module except using ZULUS generated GAF due to the pitch and plunge modes, (Q_{hh}), as well as trailing edge flap and upper spoiler oscillation, (Q_{hc}), at various frequencies.

6.1 Validation of Frequency Response due to Trailing Edge Flap Input

Shown in Figure 4 are the frequency responses at the accelerometer due to the trailing edge flap input measured by the TDT testing, computed by Waszak and ZULUS. The TDT test data was measured at a dynamic pressure (q)=125 psf. Note that the natural frequencies of the BACT wing on the PAPA flexible mount system are 3.34 Hz for the plunge mode and 5.2 Hz

for the pitch mode. However, the TDT test data shows that the frequency of the pitch mode is shifted from 5.2 Hz to approximately 4.5 Hz. Clearly, this frequency shift is due to the aeroelastic effects. Both Waszak and ZULUS results capture this frequency shift except that the results obtained by Waszak over-predict the magnitude of the peak at 4.5 Hz and ZULUS slightly under-predict this peak. At 3.0 Hz, both the Waszak and ZULUS results over-predict the magnitude of the peak, but they agree with each other well. The zigzag of the phase angle below 2 Hz in the TDT data is probably caused by the wind tunnel noise that is difficult to model by analysis. Overall speaking, the ZULUS and Waszak results correlate well with the TDT test data. However, Waszak's results were based on the wind tunnel measured aerodynamic force and moment derivatives whereas the ZULUS results were obtained by the linearized unsteady solver.

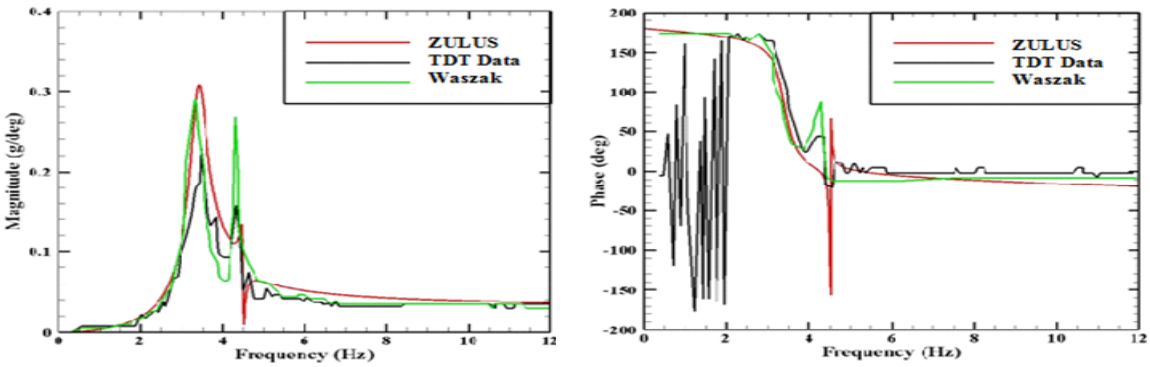

(a) Magnitude **(b) Phase Angle**

Figure 4: Frequency Response of BACT Wing for Accelerometer Output to Trailing Edge Flap Input at q=125 psf

6.2 Validation of Frequency Response due to Upper Spoiler Input

Figure 5 presents the frequency responses of the BACT wing on the PAPA flexible mount system at the accelerometer to the upper spoiler input. Again, the magnitude of the TDT data shows two peaks at 3.0 Hz and 4.5 Hz. Both Waszak's and ZULUS results capture these two peaks except that ZULUS under-predicts the magnitude at 3.0 Hz and slightly overpredicts that at 4.5 Hz. The phase angle of both Waszak's and ZULUS results agree well with that of the TDT data except at the frequencies below 2 Hz in which the TDT data was probably contaminated by the wind tunnel noise.

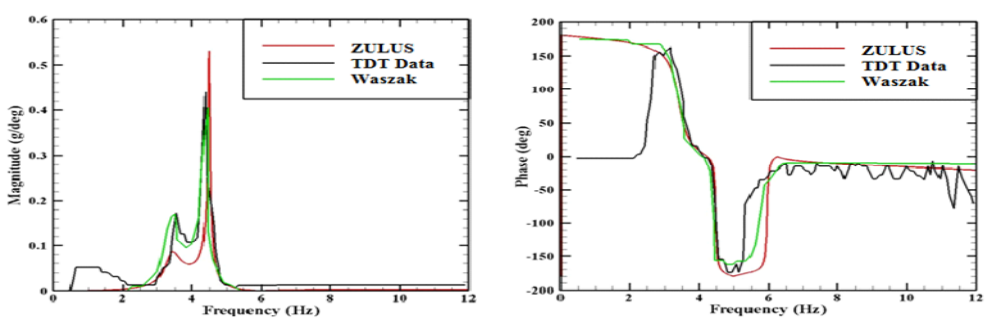

(a) Magnitude **(b) Phase Angle**

Figure 5:" Frequency Response of BACT Wing for Accelerometer Output to Upper Spoiler Input at q=125 psf.

The accurate flow field prediction of the wing pressures when a spoiler is deployed is currently beyond the capabilities of the existing ASE codes. Such a capability is urgently

needed by the aerospace industry because spoilers can be used as effective control devices for dynamic loads alleviation. For instance, Boeing 787 and Airbus A320 are equipped with a maneuver and gust load alleviation control law using the aileron and spoiler to provide the control authority that is normally obtained by an enormous amount of wind tunnel testing and flight testing to tune the control laws. This test case demonstrates that through the use of ZULUS, the amount of wind tunnel testing and flight testing required can be reduced.

7 DESCRIPTION OF THE TWIN-ENGINE TRANSPORT FLUTTER MODEL IN TDT

This Twin-Engine Transport Flutter Model (TETFM) was tested by the Boeing Company (Boeing) in TDT and is shown in Figure 6. Its TDT measured flutter boundaries at angle of attack (α)=-2° is shown in Figure 7.

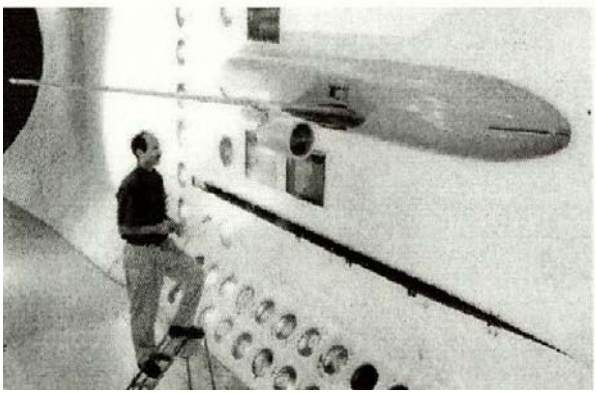

Figure 6: Twin-Engine Transport Flutter Model in TDT. (Figure Taken from Reference 13)

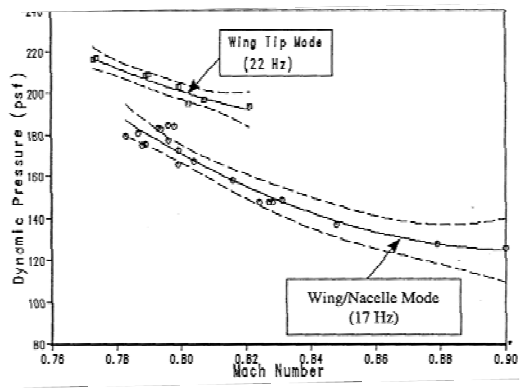

Figure 7: TDT Measured Flutter Boundaries of the Twin-Engine Transport Flutter Model. (Figure Taken from Reference 13)

During the wind tunnel testing with a Mach number below 0.83, two flutter mechanisms were measured; one at 17 Hz called the wing/nacelle mode at lower dynamic pressures and the other at 22 Hz called the wing tip mode at higher dynamic pressures. When the wing/nacelle flutter mode was first encountered at lower dynamic pressures, a low-amplitude Limit Cycle Oscillation (LCO) was observed in the TDT. Because of the low oscillation amplitude that may not damage the wind tunnel model structure, the test engineers decided to continuously increase the dynamic pressure until the wing tip flutter mode was encountered. Apparently, the wing/nacelle mode is a hump flutter mode, and the wing tip mode is an explosive flutter mode. However, at the Mach number higher than 0.83, the LCO amplitude of the wing/nacelle mode became significantly large to the extent that the test engineers stopped increasing the dynamic pressure to avoid the damage of the flutter model. Therefore, the flutter boundary of the wing tip mode was not able to be measured at Mach numbers higher than 0.83.

8 VALIDATION WITH THE TDT MEASURED FLUTTER BOUNDARY OF THE TWIN-ENGINE TRANSPORT FLUTTER MODEL

The TETFM is an ideal showcase to demonstrate the ZULUS' applicability for rapid aeroelastic analysis on complex configuration. Figure 8.(a) shows an unstructured viscous mesh for computing the viscous steady viscous flow solution using the RANS solver in FUN3D. Then, by coarsening the unstructured viscous mesh, an inviscid mesh shown in Figure 8.(b) is generated by computing the unsteady aerodynamic forces by the linearized

unsteady solver in ZULUS. The unstructured viscous mesh has 1,929,436 grids, 2,856,538 tetrahedral cells, 15,769 pyramid cells, 2,826,411 prism cells, 106,316 surface triangular cells and 12,620 surface quadrilateral cells and the unstructured inviscid mesh has 43,198 grids, 212,831 tetrahedral cells, and 36,436 surface triangular cells.

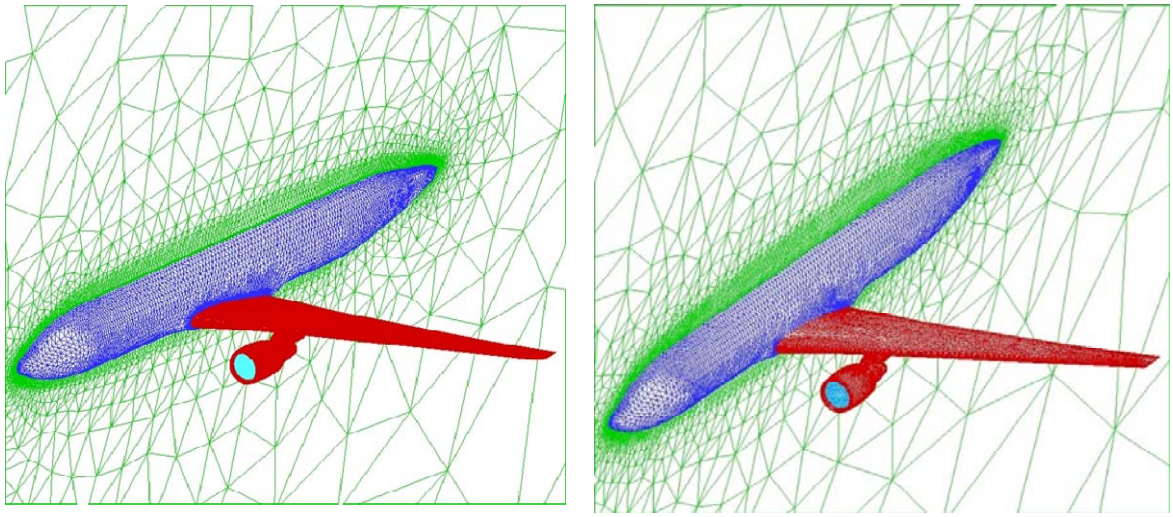

(a) Unstructured Viscous Mesh ***(b) Unstructured Inviscid Mesh***

Figure 8: Unstructured Mesh of the Twin-Engine Transport Flutter Model.

The structural model of the TETFM provided by Boeing has 12 natural modes. Using the Spline module in ZULUS, these 12 mode shapes are mapped from the structural grids to the unstructured inviscid surface mesh. The first four mapped mode shapes; namely, the first wing bending mode, the engine nacelle yaw mode, the engine nacelle pitch mode and the first wing torsion mode, are presented in Figure 9. These 12 mapped mode shapes are plugged into the transpiration boundary condition of the linearized unsteady solver to generate the $Q_{hh}(ik)$ matrix for flutter analysis using the Flutter module in ZULUS.

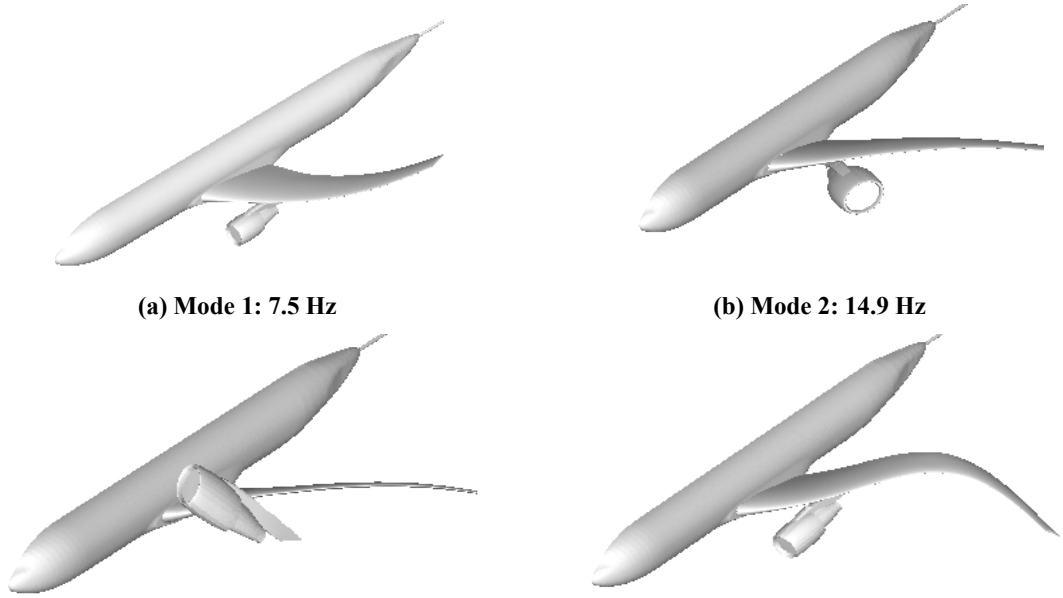

(a) Mode 1: 7.5 Hz **(b) Mode 2: 14.9 Hz**

(c) Mode 3: 19.0 Hz **(d) Mode 4: 23.3 Hz**

Figure 9: The First Four Interpolated Mode Shapes of the TETFM on the Surface Panel Model.

8.1 Viscous Steady Background Flow with and without Static Aeroelastic Effects

Using the unstructured viscous mesh shown in Figure 8.(a), the viscous steady flow solution is computed by the RANS solver in FUN3D at angle of attack (α)=-2° and at Mach numbers (M)=0.79, 0.83, 0.85, and 0.88. To solve the linearized unsteady equation, ZULUS requires the steady background flow on the unstructured inviscid mesh shown in Figure 8.(b). The viscous flow solutions at various Mach numbers computed by FUN3D are interpolated from the viscous mesh to the inviscid mesh. To validate the interpolated flow solutions, we compared the interpolated Mach contours on the inviscid mesh at M=0.88 and along 20%, 40%, 60% and 80% wing span stations to those computed on the viscous mesh. This comparison is presented in Figure 10 which shows that overall these two sets of Mach contours practically have the same distribution. These interpolated viscous flow solutions on the inviscid mesh are used as the steady background flows for the linearized unsteady solver to generate the unsteady aerodynamic forces.

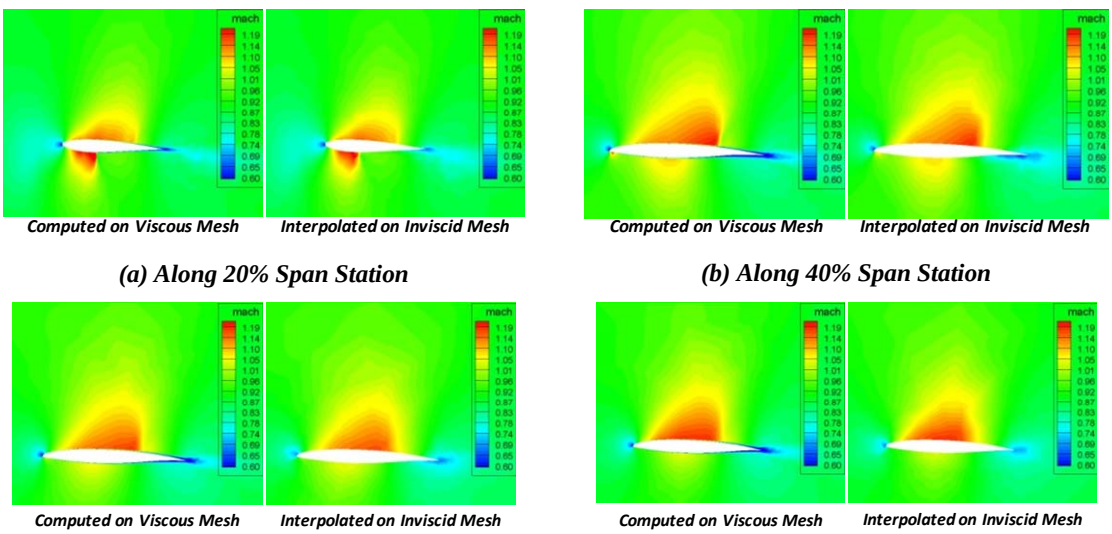

(a) Along 20% Span Station *(b) Along 40% Span Station*

(c) Along 60% Span Station *(d) Along 80% Span Station*

Figure 10: Comparison of Mach Number Contours between those Computed on Viscous Mesh and Interpolated on Inviscid Mesh at M=0.88 and α=-2°.

8.2 Convergence History of the Unsteady Aerodynamic Forces

Based on the interpolated viscous steady background flow, the unsteady aerodynamic forces due to 12 modes at six reduced frequencies (k=0.0, 0.1, 0.35, 0.6 1.0 and 1.25) are computed by the linearized unsteady solver in ZULUS for each Mach number. The total run time for each Mach number is 10 hours using 216 cores for MPI+OpenMP. Figure 11 shows the residuals convergence histories versus iteration numbers of the first four elastic modes at k=0.1 and M=0.88. The residuals of both real and imaginary parts reduce nearly four orders; verifying that the unsteady aerodynamic forces after 3000 iterations are well-converged solutions.

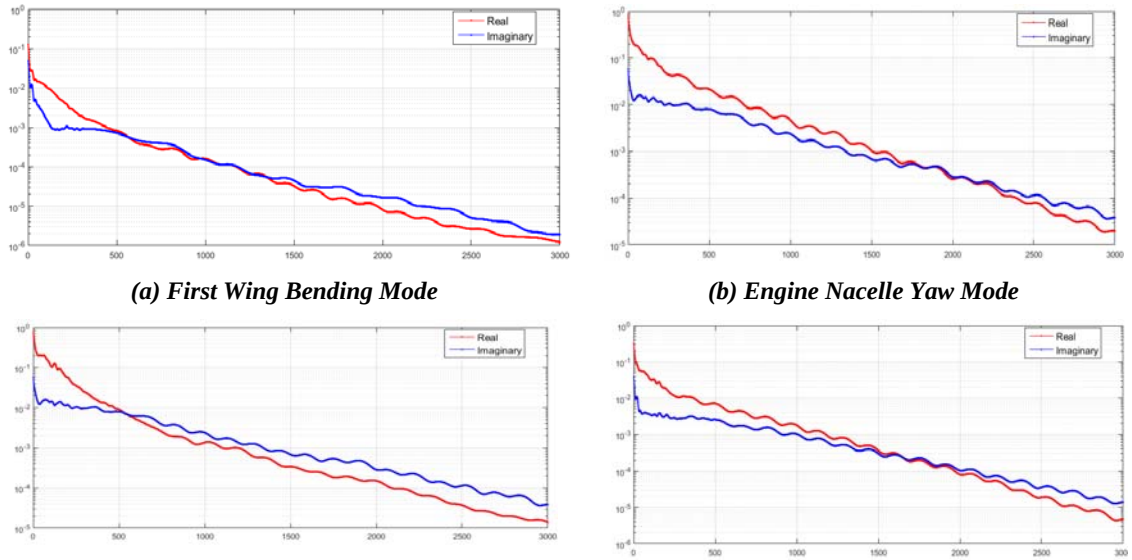

(a) First Wing Bending Mode

(b) Engine Nacelle Yaw Mode

(c) Engine Nacelle Pitch Mode

(d) First Wing Torsion Mode

Figure 11: Convergence History of the Unsteady Aerodynamic Forces at k=0.1 and M=0.88.

8.3 Investigation of Static Aeroelastic Effects on Unsteady Pressure Distributions

The linearized static aeroelastic analysis in the Trim module of ZULUS is used to "flexibilize" the interpolated viscous steady background flow. The dynamic pressures (q_∞) selected for the linearized static aeroelastic analysis are q_∞=1.2 psi at M=0.79, q_∞=1.04 psi at M=0.83, q_∞=1.04 psi at M=0.85, and q_∞=0.92 psi at M=0.88. These dynamic pressures are selected based on the flutter dynamic pressures at each Mach number measured in TDT. The steady pressure distributions with and without static aeroelastic effects along the 80% wing span station at those four Mach numbers are depicted in Figure 12. It can be seen that the magnitude of the negative pressure on the wing upper surface is significantly reduced by the static aeroelastic effects. Apparently, the static aeroelastic effects may have a major impact on the unsteady pressure distributions.

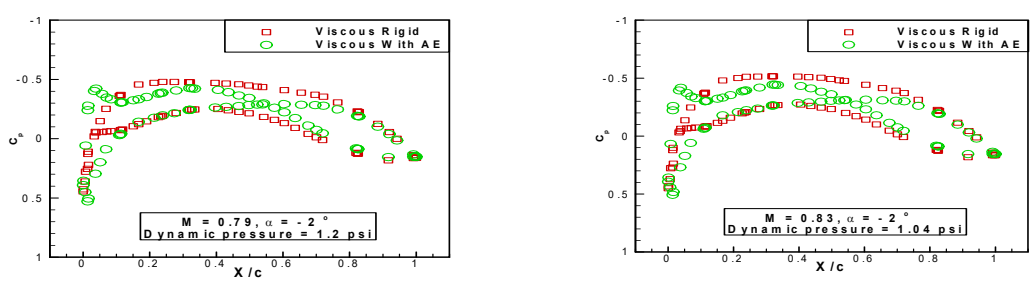

(a) M=0.79

(b) M=0.83

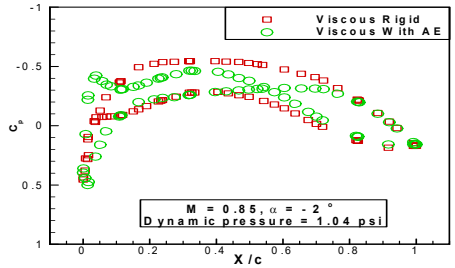

(c) M=0.85

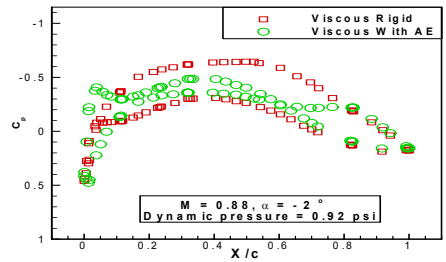

(d) M=0.88

Figure 12: Pressure Coefficients with/without static aeroelastic effects along 80% span of the Twin-Engine Transport Flutter Model.

Based on the steady viscous background flow with and without static aeroelastic effects, the real and imaginary parts of unsteady pressure distributions along 20%, 40%, 60% and 80% wing span stations due to the first wing bending mode at k=0.1 and M=0.88 are solved by the linearized unsteady solver in ZULUS and are shown in Figure 13. As expected, these two sets of unsteady pressure distribution are significantly different; showing the impact of the static aeroelastic effects on unsteady aerodynamics in transonic flows.

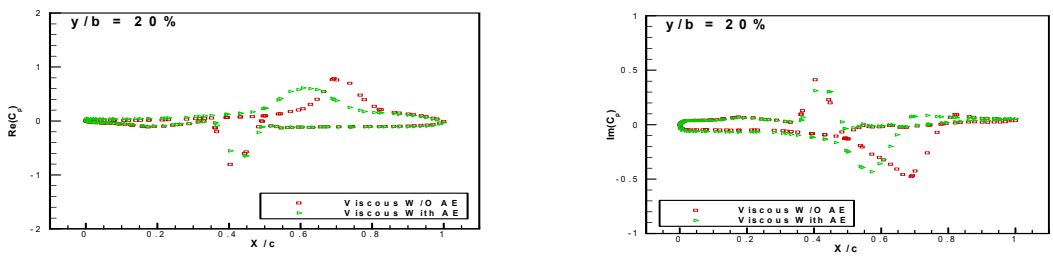

(a) Along 20% Span Station

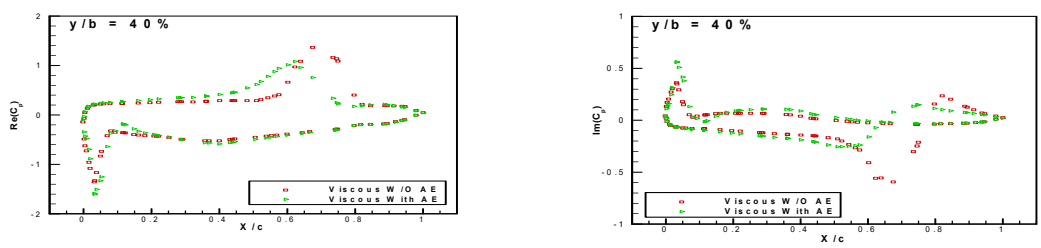

(b) Along 40% Span Station

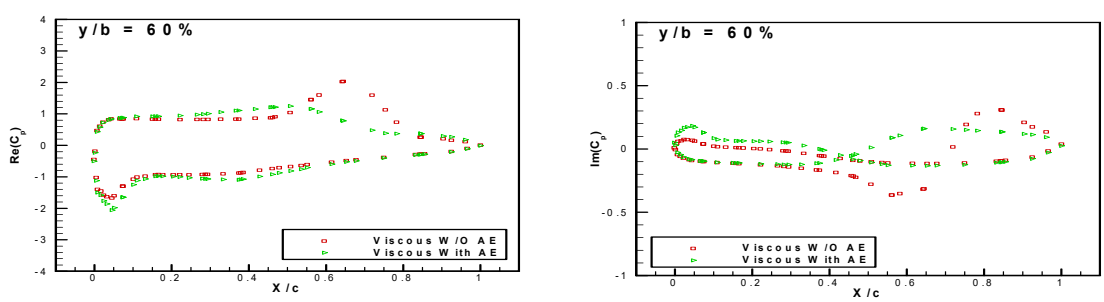

(c) Along 60% Span Station

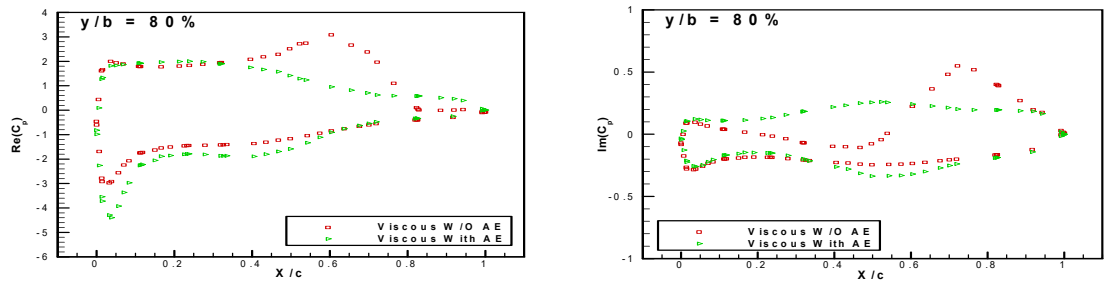

(d) Along 80% Span Station

Figure 13: Unsteady Pressure Distributions with and without Static Aeroelastic Effects due to the First Wing Bending Mode at k=0.1 and M=0.88.

8.4 Flutter Boundaries of the TETFM based on Viscous Steady Background Flow with and without Static Aeroelastic Effects

Flutter analyses are performed using the viscous generalized aerodynamic forces (GAF) with and without the static aeroelastic effects to solve the flutter equation. Figure 14 presents the flutter solutions depicted by the dynamic pressure versus damping (V-G) and dynamic pressure versus frequency (V-F) diagrams at M=0.79, 0.83, 0.85, and 0.88. At these four Mach numbers, the V-G diagrams show that two damping curves cross the zero-damping line which corresponds to two flutter modes. The flutter frequency of the first flutter mode occurs approximately at 17 Hz apparently that is the wing nacelle flutter mode observed during the TDT testing and the flutter frequency of the second flutter mode occurs approximately at 22 Hz that corresponds to the wing tip flutter mode mode observed during the TDT testing. The damping and frequency curves of the wing nacelle flutter mode computed using the GAF with static aeroelastic effects are shown by the solid red circles and those without the static aeroelastic effects are shown by the open black circles. The damping and frequency curves of the wing tip flutter mode computed using the GAF with static aeroelastic effects are shown by the solid blue squares and those without the static aeroelastic effects are shown by the open black squares. At the lower Mach numbers, the difference of the damping and frequency curves between those with and without static aeroelastic effects is small but this difference increases as the Mach number increases; showing the impact of the static aeroelastic effects on flutter results at high Mach numbers.

The horizontal dash line in the V-G diagram represents the 1% structural damping line (labeled by ζ=1%). Thus, if one percent of structural damping is assumed, the flutter dynamic pressure occurs at the crossing between the damping curves and the1% structural damping line. Otherwise, the flutter dynamic pressure occurs at the crossing between the damping curves and the zero-damping line. Because the wing nacelle flutter mode is a hump-type mode (the damping curve above the zero/one percent damping line in a narrow dynamic pressure region), the flutter dynamic pressure of the wing nacelle flutter mode is very sensitive to the amount of structural damping considered in the flutter analysis. On contrast, the damping curve of the wing tip mode is an explosive mode (the slope of the damping curve is large at the crossing), its flutter dynamic pressure is insensitive to the structural damping.

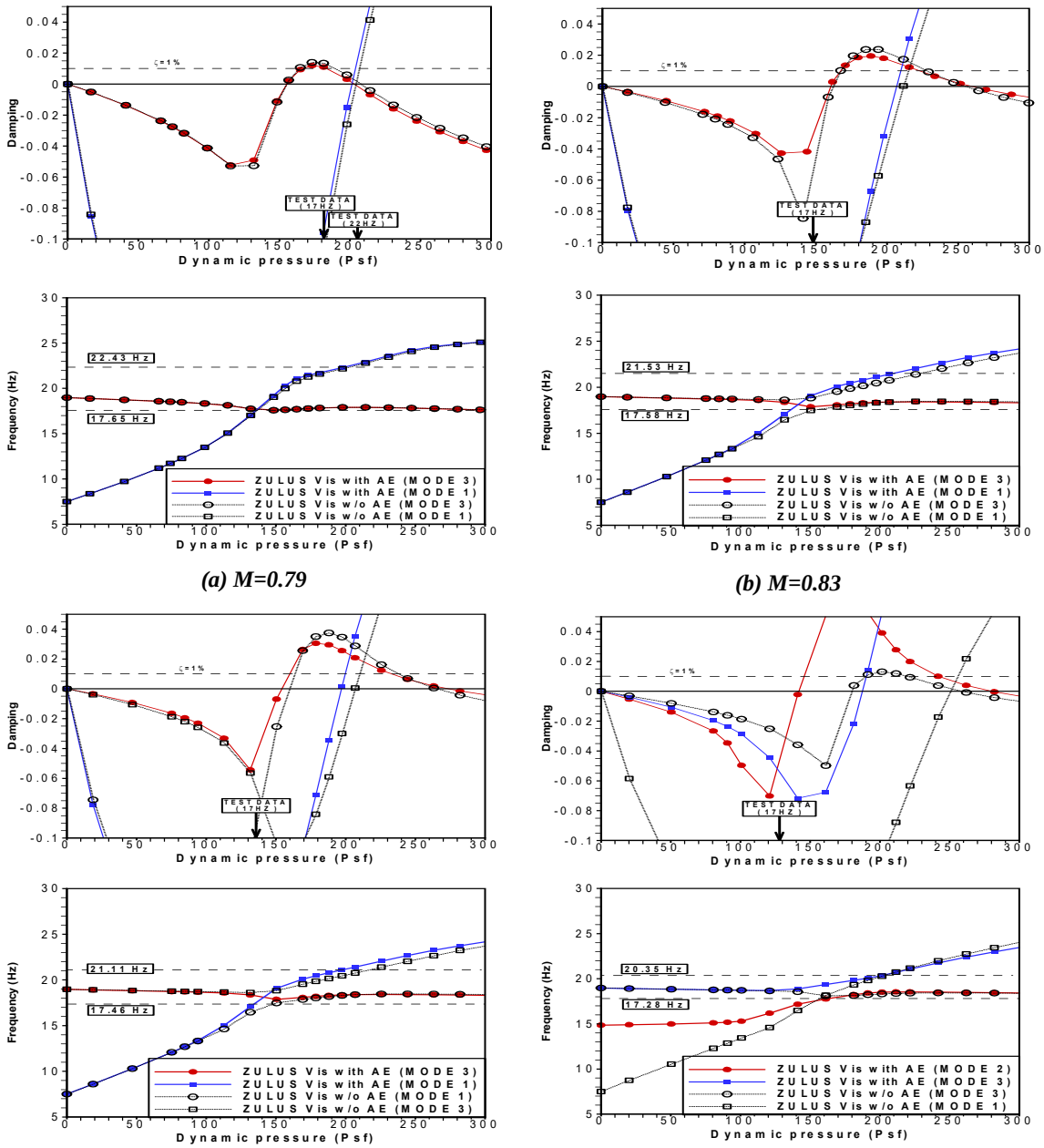

(a) M=0.79 ***(b) M=0.83***

(c) M=0.85 ***(d) M=0.88***

Figure 14: V-G and V-F Diagrams of the ZULUS Viscous Flutter Solutions for the TETFM with and without Static Aeroelastic Effects.

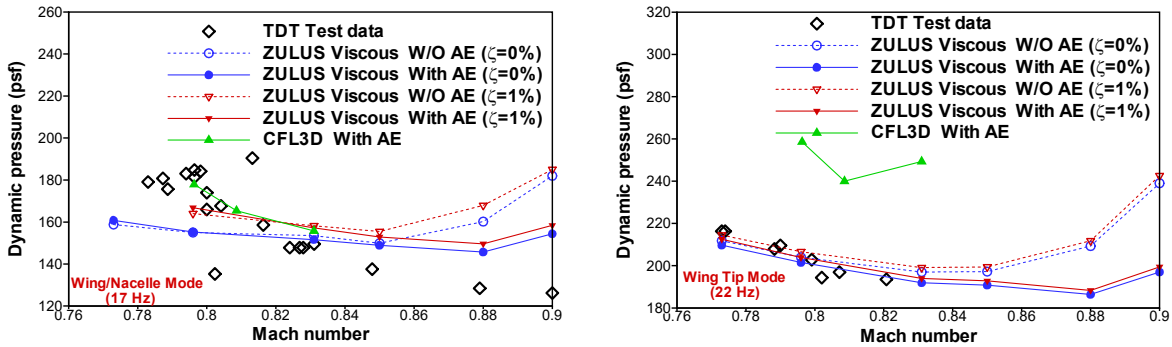

(a) Wing Nacelle Flutter Mode *(b) Wing Tip Flutter Mode*

Figure 15: Flutter Boundaries of the Twin-Engine Transport Flutter Model.

Figure 15 presents the flutter dynamic pressure versus Mach number referred to as the flutter boundary which includes six sets of flutter boundaries. The open diamonds are the flutter boundaries measured in TDT, and the solid green triangles are the CFL3D computed results [17] with static aeroelastic effects, The rest four sets of flutter boundaries are computed by ZULUS with viscous effects. The first set is the flutter boundary without the static aeroelastic effects and with zero structural damping (labeled by the open black circles). The second set is the flutter boundary with the static aeroelastic effects and with zero structural damping (labeled by the solid black circles). The third set is the flutter boundary without the static aeroelastic effects and with one percent of structural damping (labeled by the open red gradients), and the fourth set is the flutter boundary with the static aeroelastic effects and with one percent of structural damping (labeled by the solid red gradients). Among the four sets of ZULUS results, the 1% structural damping with the static aeroelastic effects is believed to be the most representative model (labeled by the solid red gradients) of the actual TETFM in TDT. The flutter boundary of this ZULUS model agrees the best with the TDT measured result for both wing nacelle and wing tip flutter modes; showing that for accurate flutter prediction all static aeroelastic, flow viscous and structural damping effects must be included in the flutter analysis.

9 CONCLUSIONS

In this work, an unstructured linearized Euler solver, called ZULUS, is developed that solves the frequency-domain linearized unsteady equation based on the steady background flow solution provided by the N-S solver. ZULUS can generate the frequency-domain generalized aerodynamic forces due to structural modes, control surface kinematic modes and gust excitation. These generalized aerodynamic forces can be directly plugged into the conventional frequency-domain flutter, aeroservoelastic (ASE) and gust analysis methodologies to generate flutter solution, ASE stability analysis, and gust loads prediction. In fact, many engineering modules in ZULUS are nearly the same as those in ZAERO except that the unsteady aerodynamic forces generator in ZAERO established by solving the unsteady potential equation is replaced by the linearized unsteady solver of ZULUS. Therefore, ZULUS is the next generation of ZAERO for rapid aeroelastic and aeroservoelastic analysis but using much more accurate unsteady aerodynamic forces than those used by ZAERO.

Because of the transpiration boundary, ZULUS can avoid the moving mesh problems associated with applying the exact N-S boundary condition that requires additional

computational resources and may encounter grid crossover problem due to large oscillating amplitude or discontinuous displacement in mode shapes.

Nowadays, the application of CFD methods for steady aerodynamic analysis is a routine practice in the aerospace industry. Therefore, the CFD mesh of a given configuration is usually available to the aeroelastic engineers so that aeroelastic analysis using ZULUS can be performed without an extensive modeling effort. Because the computational procedure of a reduced frequency-mode pair for computing its induced unsteady pressures is independent of other pairs, ZULUS can be easily parallelized to drastically reduce the computational time by computing the unsteady aerodynamic forces of all frequency-mode pairs concurrently using MPI if a large number of cores is available. Therefore, ZULUS can satisfy the computational efficiency requirement by the aerospace industry for routine aeroelastic analysis.

10 ACKNOWLEDGES

The authors would like to thank Dr. Bhatia, K.G. of Boeing for providing ZONA the CFD structured mesh and structural finite element mode of the Twin-Engine Transport Flutter Model.

11 REFERENCES

[1] Bartels, R. E., Scott, R. C., Allen, T. J.. and Sexton, B. W., "Aeroelastic Analysis of SUGAR Truss-Braced Wing Wind-Tunnel Model Using FUN3D and a Nonlinear Structural Model". AIAA-2015-1174.

[2] Anderson, W. K., and Bonhaus, D. L.: “An Implicit Upwind Algorithm for Computing Turbulent Flows on Unstructured Grids.” Compt. and Fluids, Vol. 23, No. 1, pp. 1-21, 1994.

[3] Rodden, W. P., and Bellinger, E. D., "Aerodynamic Lag Functions, Divergence and the British Flutter Method," Journal of Aircraft, Vol. 19, No. 7, 1982, pp.596-598.

[4] Chen, P.C., "A Damping Perturbation Methods for Flutter Solution: The g-Method," AIAA Journal, Vol. 38, No. 9, Sept. 2000.

[5] Albano, E. and Rodden, W. P., "A Doublet-Lattice Method for Calculating Lift Distributions on Oscillating Surfaces in Subsonic Flows," AIAA Journal, Vol. 7, No. 2 , 1969, pp. 279-285.

[6] ZAERO Version 9.0, ZONA Technology.

[7] Raveh, Daniella E., Levy, Yuval, and Karpel, Moti, "Efficient Aeroelastic Analysis Using Computational Unsteady Aerodynamics," Journal of Aircraft, Vol.38, No. 3, May-June 2001, pp. 547-556.

[8] Silva, W.A. "Simultaneous Excitation of Multiple-Input/Multiple-Output CFD-Based Unsteady Aerodynamic Systems," Journal of Aircraft, Vol. 45, No. 4, Apr. 2008, pp. 1267-1274.

[9] Kreiselmaier E., Laschka B., "Small Disturbance Euler Equations: Efficient and Accurate Tool for Unsteady Load Prediction," Journal of Aircraft, 2000. 37(5): p. 770-778

[10] Zhang, Z., Yang, S. and Chen, P. C., "Linearized Euler Solver for Rapid Frequency-Domain Aeroelastic Analysis." Journal of Aircraft, Vol. 49, No. 3, 2012, pp. 922-932.

[11] Rivera, J.A., Dansberry B.E., Bennett, R.M., Durham, M.H., and Silva, W.A., "NACA 0012 Benchmark Model Experimental Flutter Results with Unsteady Pressure Distributions," AIAA-92-2396-CP.

[12] Yang, S., Chen, P. C., and Wang, Z. "Linearized FUN3D for Rapid Aeroelastic Design and Analysis," International Forum on Aeroelasticity and Structural Dynamics, June 28-July 02, 2015, Saint Petersburg, Russia.

[13] SenGupta, G. "Comparison of TRANAIR Predictions with Flutter Model Wind Tunnel Test Data," Presented at the AFDC Meeting, Seattle, WA, October 1999.

[14] ZAERO Theoretical Manual Version 9.2, 2016, ZONA Technology Inc.

[15] Chen, P.C., Lee, H.W., and Liu, D.D., "Unsteady Subsonic Aerodynamics for Bodies and Wings with External Stores Including Wake Effect," Journal of Aircraft, Vol. 30, No. 5, Sep-Oct. 1933, p. 618-628.

[16] Waszak, M.R., "Modeling the Benchmark Active Control Technology Wind-Tunnel Model for Application to Flutter Suppression," AIAA-96-3437-CP.

[17] Hong, M.S., Bhatia, K.G., SenGupta, G., Kim, T., Kuruvila, G., Silva, W.A., Bartels, R., and Biedron, R., "Simulations of a twin-engine transport flutter model in the transonic dynamics tunnel," International Forum on Aeroelasticity and Structural Dynamics, Paper 2003-US-44, 2003.

12 COPYRIGHT STATEMENT

The authors confirm that they, and/or their company or organization, hold copyright on all of the original material included in this paper. The authors also confirm that they have obtained permission, from the copyright holder of any third party material included in this paper, to publish it as part of their paper. The authors confirm that they give permission, or have obtained permission from the copyright holder of this paper, for the publication and distribution of this paper as part of the IFASD 2017 proceedings or as individual off-prints from the proceedings.